Software-Defined Millimeter-Wave Multistatic Radar With Space-Time-Coded Orthogonal Frequency-Division Multiplexing

Weite Zhang, *Graduate Student Member, IEEE*, Yi Huang, *Graduate Student Member, IEEE*, Juan Heredia-Juesas, and Jose A. Martinez-Lorenzo, *Senior Member, IEEE*

***Abstract*— High-performance millimeter-wave (mm-wave) multiple-in-multiple-out (MIMO) radars have been using efficient multiplexing with increasingly complicated radar waveforms, where conventional hardware architectures suffer from inevitably high design complexity and cost. This article presents a new software-defined mm-wave multistatic imaging system which provides great efficiency and flexibility to generate and process complicated radar waveforms. A general system block diagram and its signal model are proposed to use space-time-coded orthogonal frequency-division multiplexing (OFDM) for simultaneous MIMO transmission at the same time and frequency. The space-time coding (STC) is designed based on the Hadamard matrix which allows simple decoupling and decoding for imaging processing. A radar prototype is designed to validate the proposed system architecture, which operates at 83.5 GHz with a frequency bandwidth of 4.8 GHz. The mm-wave front-end consists of a metal-printed 8-by-8 waveguide array with a small element-separation of 9 mm to form 64 virtual channels for three-dimensional imaging. Experimental results show good imaging performance, giving great potential to design future cost-effective high-performance mm-wave imaging with efficient multiplexing.**

***Index Terms*— Efficient multiplexing, millimeter-wave (mm-wave), multiple-in-multiple-out (MIMO) radar, multistatic, orthogonal frequency-division multiplexing (OFDM), software-defined, space-time coding (STC), 3-D imaging.**

I. Introduction

CONVENTIONAL millimeter-wave (mm-wave) multiple-in multiple-out (MIMO) radars use time-division multiplexing, or frequency-division multiplexing, or both [1]–[3], where only one transmitter can be active at the same time and frequency. Such multiplexing approaches can lead to low receiving signal-to-noise ratio (SNR). High-performance mm-wave radars have been explored to use more and more efficient multiplexing by designing increasingly complicated radar waveforms. One approach is to adopt space-time coding (STC) for simultaneous MIMO transmission [4]–[6] at the same time and frequency, which can help achieve higher receiving SNR and faster image formation rate. Another approach is to use orthogonal frequency-division multiplexing (OFDM) [7]–[9] which can increase the spectral efficiency of radar systems where more measurement samples per frequency bandwidth can be obtained. Nevertheless, as the complexity of radar waveforms increases, conventional mm-wave imaging systems inevitably suffer from high hardware design complexity and cost, especially when the MIMO size is large.

Software-defined radio (SDR) is a radio frequency (RF) transceiver, capable of performing traditional hardware functionalities, such as mixers, filters, modulators, or demodulators, by means of software [10]. Due to the great flexibility afforded by software, software-defined mm-wave (SDMMW) radars have been developed to achieve efficient multiplexing. For instance, a 77-GHz single-channel SDMMW radar is proposed for range-Doppler measurement [11], [12], which is integrated on printed circuit boards (PCBs), where an OFDM waveform with a bandwidth of 200 MHz is used. Another integrated 77-GHz SDMMW radar with a 4×4 multistatic linear array is designed for range-Doppler measurement [4], [13]. The radar uses code-division multiplex-based phase-coded frequency-modulated continuous wave (FMCW) with a chirp bandwidth of 250 MHz, where simultaneous MIMO transmission is feasible. SDMMW radars have also been implemented using cost-effective commercial SDRs, where additional RF and mm-wave modules are required for intermediate frequency (IF) to mm-wave transition. Such modularized radar designs outperform integrated ones in terms of the cost and design period. As an example, an SDMMW radar using a commercial SDR with four transmitting and four receiving channels is proposed [14], where each channel is connected to a 32-element phased array to achieve a good angular resolution. Considering no frequency synthesis is used and the design of high sampling rate digital-to-analog (DA) and analog-to-digital (AD) converters is very expensive and difficult, the aforementioned SDMMW radars have limited frequency bandwidth, typically within several

Manuscript received September 21, 2021; revised November 10, 2021; accepted November 16, 2021. Date of publication December 28, 2021; date of current version March 4, 2022. This work was supported in part by the NSF Career Program under Award 1653671 and in part by the U.S. Department of Homeland Security under Award 2013-ST-061-ED0001. *(Corresponding author: Jose A. Martinez-Lorenzo.)*

Weite Zhang and Yi Huang are with the Department of Electrical and Computer Engineering, Northeastern University, Boston, MA 02115 USA (e-mail: zhang.weit@northeastern.edu; huang.yi1@northeastern.edu).

Juan Heredia-Juesas and Jose A. Martinez-Lorenzo are with the Department of Electrical and Computer Engineering and the Department of Mechanical and Industrial Engineering, Northeastern University, Boston, MA 02115 USA (e-mail: j.herediajuesas@northeastern.edu; j.martinez-lorenzo@northeastern.edu).

Color versions of one or more figures in this article are available at https://doi.org/10.1109/TMTT.2021.3134182.

Digital Object Identifier 10.1109/TMTT.2021.3134182

hundred of megahertz [15], [16], corresponding to low range resolution.

To perform 3-D imaging with good angular and range resolution, another SDMMW phased-array radar, operating at 28 GHz with a tunable external local oscillator (LO), is proposed [17], [18]. The radar hardware consists of two identical 64-element phased arrays. One is connected to the transmitting channel and the other one is connected to the receiving channel. The commercial SDRs are used to generate the OFDM waveform with a bandwidth of 100 MHz. The wide bandwidth measurement over 1 GHz is implemented by stitching multiple OFDM waveforms at different LO frequencies. Note that such phased arrays suffer from high hardware design complexity and cost [19] to integrate many physical antenna elements, which can be avoided if using multistatic arrays. Specifically, to achieve an equivalent number of virtual MIMO channels, the number of physical antenna elements of a phased array ($N \times M$ transceivers) will be much larger than that of a multistatic array (N transmitters $+$ M receivers), especially when N and M are large.

This article presents a new SDMMW multistatic radar design using cost-effective commercial SDRs. The main novelty and contribution are summarized as follows.

1) A general block diagram is proposed to design the SDMMW multistatic radar with massive MIMO capability, which makes use of cost-effective commercial SDRs and additional RF and mm-wave modules. The software flexibility provided by the SDRs can greatly help reduce hardware design complexity, compared with conventional mm-wave imaging architectures. A tunable external LO is used as stepped FMCW for wide-band frequency synthesis with reduced instantaneous bandwidth requirement on the IF. Also, the modularized hardware architecture is fully scalable for a large MIMO array design. Such a radar architecture can enable high-resolution 3-D imaging.
2) The corresponding signal model and imaging theory are developed, where the radar waveform is specifically designed to use STC OFDM for simultaneous MIMO transmission at the same time and frequency. Note that such a waveform is widely used in 4G/5G wireless communications [20] but has not been explored in mm-wave imaging with a large MIMO size [6]. In this work, the STC is designed based on the Hadamard matrix [21] which allows simple decoupling and decoding for imaging processing.
3) An experimental SDMMW radar prototype is designed to perform STC OFDM in an 8-by-8 multistatic configuration which forms 64 virtual channels. The radar operates at 83.5 GHz with a frequency bandwidth of 4.8 GHz. To achieve a small element separation and reduce the sidelobe effect, a WR-12 waveguide array is specially designed by metal printing. 3-D imaging experiments are carried out to show good performance, giving great potential to design future cost-effective high-performance mm-wave imaging with efficient multiplexing. To our best knowledge, this is the first SDMMW multistatic radar system with no less than 64 measurement channels (8 Txs and 8 Rxs) for 3-D imaging applications.

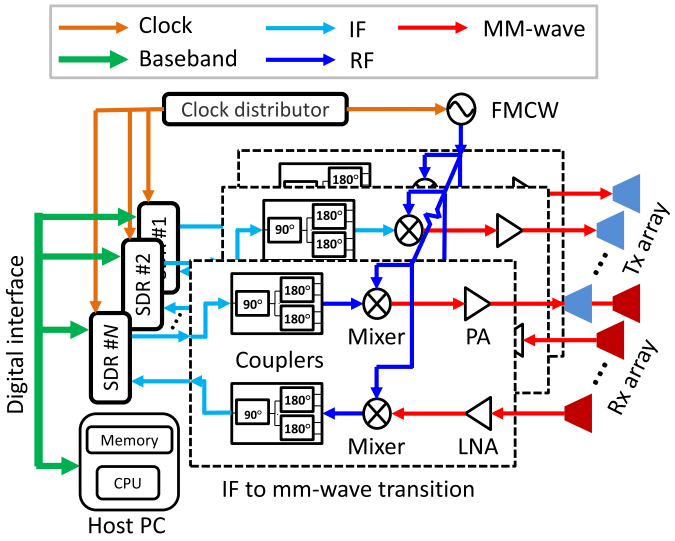

Fig. 1. General block diagram to design an SDMMW multistatic radar with massive MIMO capability. SDR: software-defined radio. PA: power amplifier. LNA: low-noise amplifier. Tx: transmitter. Rx: receiver. CPU: central processing unit. IF: intermediate frequency. RF: radio frequency. MM-wave: millimeter-wave. FMCW: frequency-modulated continuous wave. PC: personal computer.

The rest of this article is organized as follows. Section II shows the general block diagram of the SDMMW radar. Section III presents the corresponding signal model, imaging theory, and receiving SNR analysis. Section IV demonstrates the radar prototype, hardware/software specifications, and 3-D imaging results. The conclusion is drawn in Section V.

II. General Block Diagram

The general block diagram of the SDMMW multistatic radar with massive MIMO capability is presented in Fig. 1, which makes use of commercial SDRs and additional RF and mm-wave modules. In each transmitter (Tx) chain, the STC OFDM waveform is generated at the digital baseband in the host personal computer (PC), which is then sent to the corresponding SDR module through a high-speed digital interface (e.g. USB 3.0). The SDR performs DA conversion and up-converts the radar waveform. The IF output will pass through a single-to-differential converter that consists of one 90° coupler and two 180° couplers. Note that the use of the single-to-differential coupler may not be a necessity; however, it can help the radar immune to thermal drift and external electromagnetic interference. The differential outputs are then fed to Tx mm-wave mixer which also takes in the coherently distributed stepped FMCW generated by the external LO module. The mm-wave output is amplified by a power amplifier (PA) and radiated from the Tx.

Similarly, in each receiver (Rx) chain, the Rx first captures the reflected mm-wave signal which essentially represents the coupled and delayed combination of the simultaneously transmitted radar waveforms. The received mm-wave signal is amplified by a lower-noise amplifier (LNA) and down-converted by mixing with coherent FMCW. The IF output

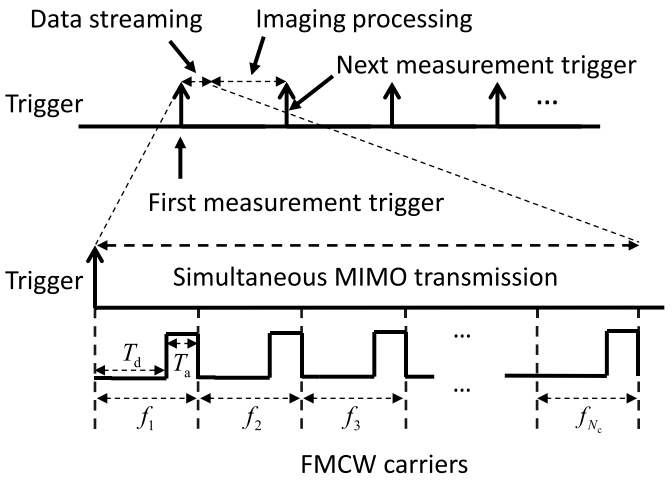

Fig. 2. Hardware operation sequence of the SDMMW radar, where simultaneous MIMO transmission at the same frequency and time is enabled.

will pass through a differential-to-single converter and is further down-converted to the analog baseband waveform and digitized by AD converter in the SDR. The waveform samples at the digital baseband are then streamed to the host PC for 3-D imaging processing. Note that an external clock distributor is used to provide baseband timing and clock reference for all the associated hardware modules.

Fig. 2 shows the hardware operation sequence of the SDMMW imaging system. At the arrival of each measurement trigger, the external LO will start a full FMCW sweep from the start frequency f_1 to the end frequency f_{N_c}, where N_c is the number of FMCW frequency steps. The SDRs will simultaneously perform data streaming in all Tx and Rx channels during each frequency step. Note that the frequency step time consists of dwell time T_d and data streaming time T_a. T_d is to ensure a stable phase lock loop at each FMCW step. The radar waveform is duplicated at each FMCW frequency step, and imaging processing is performed immediately after each full FMCW sweep cycle.

III. Signal Model and Imaging Theory

A. Signal Model

The signal model of the SDMMW multistatic radar is presented in this section. Although arbitrary waveform generation is possible, in this work, the radar waveform is designed to use STC OFDM for simultaneous MIMO transmission at the same time and frequency. Note that such a waveform is widely used in 4G/5G wireless communications [20] but has not been explored in mm-wave imaging with a large MIMO size. The use of STC OFDM can provide better receiving SNR and higher spectral efficiency, compared with conventional time-division or frequency-division imaging systems.

In this work, the space-time codes are specifically constructed based on the Hadamard matrix [21] which allows simple decoupling and decoding to retrieve the transfer function of each virtual channel for imaging processing. An example of STC OFDM with four Txs and four Rxs is depicted in Fig. 3, where the ith Tx transmits an OFDM sequence of four symbols with orthogonal space-time codes, either -1 or $+1$,

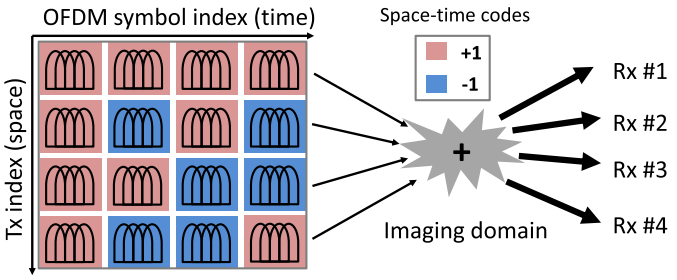

Fig. 3. Example of STC OFDM with four Txs and four Rxs, where the ith Tx transmits an OFDM sequence of four symbols with orthogonal space-time codes. Each Rx receives a waveform which is a coupled and delayed combination of the simultaneously transmitted STC OFDM waveforms.

which is designed based on the ith row of the Hadamard matrix. Each Rx receives a waveform which is a coupled and delayed combination of the simultaneously transmitted STC OFDM waveforms from different Txs.

Assume the total number of Txs and Rxs is N_t and N_r, respectively, and n_tth Tx and n_rth Rx are located at $\mathbf{r}_{n_t}$ and $\mathbf{r}_{n_r}$, respectively. The original baseband OFDM waveform without STC is expressed as

$$s_0(t) = \sum_{n_{subc}=1}^{N_{subc}} c_{n_{subc}} e^{j2\pi (n_{subc} - N_{subc}/2 - 1)\Delta f_{subc} t} \tag{1}$$

where N_{subc} is the number of subcarriers of each OFDM symbol; $c_{n_{subc}}$ is the pseudo-noise (pn) code [22], either -1 or $+1$, on the n_{subc}th subcarrier; $\Delta f_{subc} = (f_s/N_{subc})$ is the frequency spacing between two adjacent subcarriers, with f_s being the sampling rate of the baseband AD/DA converters; and $T_s = (1/\Delta f_{subc})$ is the duration of each OFDM symbol.

The STC OFDM waveform requires the number of OFDM symbols N_s for each Tx antenna at each FMCW carrier to be equal to the number of Txs, namely, $N_s = N_t$. Also, the N_s STC OFDM symbols are duplicated at each FMCW carrier frequency f_{n_c}, $n_c \in [1, N_c]$. Thus, the baseband STC OFDM sequence for the n_tth Tx can be written as.

$$s^{\text{Tx-BB}}_{n_c,n_t,n_s}(t) = m_{n_t,n_s} \text{rect}_{n_c,n_s}(t) s_0(t), \tag{2}$$

where m_{n_t,n_s} is the Hadamard-based space-time code (either -1 or $+1$) at the n_sth OFDM symbol at the n_tth Tx, and $\text{rect}_{n_c,n_s}(t)$ is the rectangular function representing the transmission window of the n_sth STC OFDM symbol at the n_cth FMCW carrier, namely

$$\text{rect}_{n_c,n_s}(t) = \text{rect}\left(\frac{t - (n_c - 1)N_s T_s - (n_s - 1/2)T_s}{T_s}\right) \tag{3}$$

where $\text{rect}(\cdot)$ is the standard rectangular function [23]. Accordingly, the IF output at the SDR is

$$s^{\text{Tx-IF}}_{n_c,n_t,n_s}(t) = e^{jf_0^{\text{IF}} t} s^{\text{Tx-BB}}_{n_c,n_t,n_s}(t) \tag{4}$$

where f_0^{IF} is a constant IF frequency for all the Tx and Rx channels.

Considering a stepped FMCW is generated by the external LO module, the n_cth FMCW carrier can be expressed as

$$s^{\text{FMCW}}_{n_c}(t) = e^{j2\pi[f_1 + (n_c - 1)\Delta f_c]t + \varphi_0} \tag{5}$$

where f_1 is the FMCW start frequency; Δf_c is the FMCW frequency step size; and φ_0 is the constant initial phase at each frequency step. Thus, the transmitted mm-wave at the n_tth Tx antenna can be expressed as

$$s^{\mathrm{Tx-MMW}}_{n_c,n_t,n_s}(t) = s^{\mathrm{Tx-IF}}_{n_c,n_t,n_s}(t) s^{\mathrm{FMCW}}_{n_c}(t). \tag{6}$$

Considering a point scatter is located at $\mathbf{r}_o$ in the imaging domain, the received mm-wave at the n_rth Rx will be a delayed and attenuated version of the transmitted one, namely

$$s^{\mathrm{Rx-MMW}}_{n_c,n_r,n_t,n_s}(t) = \frac{1}{d_{n_t} d_{n_r}} s^{\mathrm{Tx-MMW}}_{n_c,n_t,n_s}\left(t - \Delta t_{n_r,n_t}\right) \tag{7}$$

where $d_{n_t} = |\mathbf{r}_{n_t} - \mathbf{r}_o|$ and $d_{n_r} = |\mathbf{r}_o - \mathbf{r}_{n_r}|$ are the forward and backward propagation distance, respectively, and $\Delta t_{n_r,n_t}$ is the total propagation delay, namely

$$\Delta t_{n_r,n_t} = \frac{2\left(d_{n_t} + d_{n_r}\right)}{c_0} \tag{8}$$

where c_0 is the speed of the light in free space.

Since all the N_t Txs are transmitting simultaneously, the total received waveform by the n_rth Rx will be

$$s^{\mathrm{Rx-MMW}}_{n_c,n_r,n_s}(t) = \sum_{n_t=1}^{N_t} s^{\mathrm{Rx-MMW}}_{n_c,n_r,n_t,n_s}(t) \tag{9}$$

which will then be down-converted by mixing with the coherent FMCW, giving rise to IF input at the SDR. Thus, the received analog baseband is retrieved after IF down-conversion, namely

$$\begin{aligned} s^{\mathrm{Rx-BB}}_{n_c,n_r,n_s}(t) &= s^{\mathrm{Rx-MMW}}_{n_c,n_r,n_s}(t)\left\{s^{\mathrm{FMCW}}_{n_c}(t)\right\}^*\left\{e^{jf_0^{\mathrm{IF}}t}\right\}^* \\ &= \sum_{n_t=1}^{N_t} \frac{1}{d_{n_t} d_{n_r}} e^{-j2\pi[f_1+(n_c-1)\Delta f_c]\Delta t_{n_r,n_t}} \\ &\quad \times s^{\mathrm{Tx-BB}}_{n_c,n_t,n_s}\left(t - \Delta t_{n_r,n_t}\right) \times e^{-j2\pi f_0^{\mathrm{IF}} \Delta t_{n_r,n_t}} \end{aligned} \tag{10}$$

where $\{\cdot\}^*$ denotes the complex conjugate operation, representing the frequency down-conversions in the Rx chain.

To construct the measurement vector for 3-D imaging, $s^{\mathrm{Rx-BB}}_{n_c,n_r,n_s}(t)$ needs to be digitized and transformed to the frequency domain. Thus, (10) can be rewritten in a matrix form in the frequency domain as

$$\mathbf{S}^{\mathrm{Rx-BB}}_{n_c,n_{\mathrm{subc}}}\big|_{N_r\times N_s} = \mathbf{H}_{n_c,n_{\mathrm{subc}}}\big|_{N_r\times N_t} \mathbf{S}^{\mathrm{Tx-BB}}_{n_c,n_{\mathrm{subc}}}\big|_{N_t\times N_s} \tag{11}$$

where $N_r = N_t = N_s$; $\mathbf{S}^{\mathrm{Tx-BB}}_{n_c,n_{\mathrm{subc}}}$ is the transmitted STC OFDM matrix at the digital baseband, whose (n_t, n_s)th entry is $c_{n_{\mathrm{subc}}} m_{n_t,n_s}$; $\mathbf{S}^{\mathrm{Rx-BB}}_{n_c,n_{\mathrm{subc}}}$ is the received STC OFDM matrix at the digital baseband; and $\mathbf{H}_{n_c,n_{\mathrm{subc}}}$ is the channel response matrix with its (n_r, n_t)th entry defined by $h_{n_r,n_t,n_c,n_{\mathrm{subc}}}$ which represents the transfer function between the n_rth Rx and the n_tth Tx, namely

$$h_{n_r,n_t,n_c,n_{\mathrm{subc}}} = \frac{1}{d_{n_t} d_{n_r}} e^{-j2\pi f_{n_c,n_{\mathrm{subc}}} \frac{2\left(d_{n_t}+d_{n_r}\right)}{c_0}} \tag{12}$$

where $f_{n_c,n_{\mathrm{subc}}}$ is the synthesized carrier frequency, defined as

$$\begin{aligned} f_{n_c,n_{\mathrm{subc}}} = f_1 &+ (n_c - 1)\Delta f_c + f_0^{\mathrm{IF}} \\ &+ (n_{\mathrm{subc}} - N_{\mathrm{subc}}/2 - 1)\Delta f_{\mathrm{subc}}. \end{aligned} \tag{13}$$

B. Imaging Theory

Considering the STC is designed based on the Hadamard matrix, $\mathbf{S}^{\mathrm{Tx-BB}}_{n_c,n_{\mathrm{subc}}}$ in (11) can be rewritten as

$$\mathbf{S}^{\mathrm{Tx-BB}}_{n_c,n_{\mathrm{subc}}} = c_{n_{\mathrm{subc}}}\mathbf{M} \tag{14}$$

where $\mathbf{M}$ denotes the Hadamard matrix with an order of N_t. Note that the rows of $\mathbf{M}$ form a mutually orthogonal set of codes, namely, $\mathbf{M}\mathbf{M}^{\mathrm{T}} = N_t\mathbf{I}$, $\mathbf{I}$ being the identity matrix and $(\cdot)^{\mathrm{T}}$ being the matrix transpose operation. Thus, the inversion of $\mathbf{M}$ is simply its transpose with a constant weight, namely

$$\mathbf{M}^{-1} = \frac{1}{N_t}\mathbf{M}^{\mathrm{T}}. \tag{15}$$

Therefore, $\mathbf{S}^{\mathrm{Rx-BB}}_{n_c,n_{\mathrm{subc}}}$ can be decoupled and decoded easily by the following matrix multiplication:

$$\mathbf{H}_{n_c,n_{\mathrm{subc}}} = \frac{1}{c_{n_{\mathrm{subc}}} N_t}\mathbf{S}^{\mathrm{Rx-BB}}_{n_c,n_{\mathrm{subc}}}\mathbf{M}^{\mathrm{T}} \tag{16}$$

which gives rise to the estimated channel response matrix at each OFDM subcarrier at each FMCW carrier. Thus, the measurement vector $\mathbf{g}_{\mathrm{subc}}|_{N_g\times 1}$ at the n_{subc}th OFDM subcarrier can be constructed by cascading and vectorizing all $\mathbf{H}_{n_c,n_{\mathrm{subc}}}$, $\forall n_c \in [1, N_c]$, namely

$$\mathbf{g}_{n_{\mathrm{subc}}} = \mathrm{vec}\left(\begin{bmatrix} \mathbf{H}_{1,n_{\mathrm{subc}}} & \mathbf{H}_{2,n_{\mathrm{subc}}} & \cdots & \mathbf{H}_{N_c,n_{\mathrm{subc}}} \end{bmatrix}\right) \tag{17}$$

where $N_g = N_r \times N_t \times N_c$; and $\mathrm{vec}(\cdot)$ denotes the vectorization operation on a matrix.

To perform 3-D object imaging, the sensing matrix $\mathbf{A}_{\mathrm{subc}}|_{N_g\times N_p}$ at the n_{subc}th OFDM subcarrier has to be computed according to MIMO array arrangement and imaging domain configuration, where N_p is the total number of pixels with unknown reflectivity in the imaging domain. Denote $\mathbf{E}^{\mathrm{Tx}}_{n_t,n_c,n_{\mathrm{subc}}}$ and $\mathbf{E}^{\mathrm{Rx}}_{n_r,n_c,n_{\mathrm{subc}}}$ as the electric field distribution on the n_tth Tx aperture and the n_rth Rx aperture, respectively, at the carrier frequency defined in (13). Note that both Tx and Rx apertures are the standard WR-12 ports in the later experiments and their electric field distributions can be computed by full-wave simulations.

Using the surface equivalence theorem [24], the magnetic current sources $\mathbf{M}^{\mathrm{Tx}}_{n_t,n_c,n_{\mathrm{subc}}}$ and $\mathbf{M}^{\mathrm{Rx}}_{n_r,n_c,n_{\mathrm{subc}}}$ on the Tx and Rx apertures can be calculated as follows:

$$\begin{aligned} \mathbf{M}^{\mathrm{Tx}}_{n_t,n_c,n_{\mathrm{subc}}} &= -2\mathbf{n}_0 \times \mathbf{E}^{\mathrm{Tx}}_{n_t,n_c,n_{\mathrm{subc}}} \\ \mathbf{M}^{\mathrm{Rx}}_{n_r,n_c,n_{\mathrm{subc}}} &= -2\mathbf{n}_0 \times \mathbf{E}^{\mathrm{Rx}}_{n_r,n_c,n_{\mathrm{subc}}} \end{aligned} \tag{18}$$

where $\mathbf{n}_0$ is the outward normal vector at the Tx/Rx aperture. Thus, the Tx electric field $\mathbf{E}^{\mathrm{RoI}}_{n_t,n_c,n_{\mathrm{subc}},n_p}$ and the Rx electric field $\mathbf{E}^{\mathrm{RoI}}_{n_r,n_c,n_{\mathrm{subc}},n_p}$ in the imaging domain (or region of interest, RoI) can be computed using the near-field integration over the magnetic current sources, and the sensing matrix $\mathbf{A}$ can be computed using the first-order Born approximation [25], namely

$$\mathbf{A}_{n_r,n_t,n_c,n_{\mathrm{subc}},n_p} = \mathbf{E}^{\mathrm{RoI}}_{n_t,n_c,n_{\mathrm{subc}},n_p} \cdot \mathbf{E}^{\mathrm{RoI}}_{n_r,n_c,n_{\mathrm{subc}},n_p}. \tag{19}$$

Thus, the sensing matrix $\mathbf{A}_{\mathrm{subc}}|_{N_g\times N_p}$ can be constructed by cascading and reshaping the corresponding $\mathbf{A}_{n_r,n_t,n_c,n_{\mathrm{subc}},n_p}$ at the n_{subc}th OFDM subcarrier.

The imaging reconstruction can be described to solve the inverse problem of $\mathbf{Au} + \mathbf{n} = \mathbf{g}$ where $\mathbf{A}$ is the sensing matrix, $\mathbf{u}$ is the unknown reflectivity of the pixels in the RoI, representing the target profile in 3-D; $\mathbf{n}$ is the additive thermal noise; and $\mathbf{g}$ is the measurement vector. Such an inverse problem can be solved by norm-1 or norm-2-based regularization and iterative methods to obtain an optimized solution, however, at the expense of a high computational complexity. This article adopts a computationally efficient method based on the matched filter $\mathbf{u} = \mathbf{A}^{\dagger}\mathbf{g}$, which is commonly used in synthetic aperture radar (SAR) [26], where $(\cdot)^{\dagger}$ is the transpose conjugate of a matrix. Note that the matched filter needs to be revised here to consider all the OFDM subcarriers, leading to the following reconstruction algorithm:

$$\mathbf{u} = \frac{1}{N_{\text{subc}}} \sum_{n_{\text{subc}}=1}^{N_{\text{subc}}} \mathbf{A}^{\dagger}_{n_{\text{subc}}} \mathbf{g}_{n_{\text{subc}}} \tag{20}$$

which essentially performs imaging reconstructions at all the OFDM subcarriers.

In this revised matched filter, the total number of complex multiplications is $N_{\text{subc}} N_{\text{p}} N_{\text{g}}$, and the total number of complex additions is $N_{\text{subc}} N_{\text{p}} (N_{\text{g}} - 1) + N_{\text{p}} (N_{\text{subc}} - 1)$. Consequently, the total number of complex operations, namely, the overall computational complexity (CC), of the imaging processing algorithm is

$$\text{CC} = N_{\text{subc}} N_{\text{p}} \left(2N_{\text{g}} - 1\right) + N_{\text{p}} (N_{\text{subc}} - 1). \tag{21}$$

C. Receiving SNR Enhancement by STC

In this section, the theoretical receiving SNR enhancement by STC, in comparison to conventional TDM, is analyzed. The forward model of either STC or TDM with the thermal (Gaussian white) noise vector $\mathbf{n}$ at each Rx and each frequency can be described as

$$\mathbf{s} = \mathbf{hC} + \mathbf{n} \tag{22}$$

where $\mathbf{s}|_{1\times N_{\text{t}}}$ is the raw received vector at the Rx; $\mathbf{C}|_{N_{\text{t}}\times N_{\text{t}}}$ is the transmitted coding matrix based on either STC or TDM; $\mathbf{n}|_{1\times N_{\text{t}}}$ is the thermal noise; and $\mathbf{h}$ is the transfer function of the Tx–Rx pair which will be used to construct the measurement vector for imaging reconstruction. Thus, the estimated $\tilde{\mathbf{h}}$ can be expressed as

$$\begin{aligned} \tilde{\mathbf{h}} &= \mathbf{sC}^{-1} \\ &= \mathbf{h} + \mathbf{nC}^{-1}. \end{aligned} \tag{23}$$

Note that in the STC case, $\mathbf{C}$ is the Hadamard matrix $\mathbf{M}$, as described in (14) and (15), and thus the equivalent thermal noise vector will be $\mathbf{n}_{\text{STC}} = \mathbf{nM}^{-1}$. While in the TDM case, $\mathbf{C}$ is an identical matrix $\mathbf{I}$, and the equivalent thermal noise vector will be $\mathbf{n}_{\text{TDM}} = \mathbf{nI}^{-1}$.

Assuming the variance of the thermal noise is σ_0^2, the equivalent noise variances of the STC and TDM cases will be $\sigma^2_{\text{STC}} = (\sigma_0^2/N_{\text{t}})$ and $\sigma^2_{\text{TDM}} = \sigma_0^2$, respectively. Thus, the receiving SNR enhancement by STC in the proposed SDMMW imaging system, in comparison to the conventional TDM, is

$$\begin{aligned} \frac{\text{SNR}_{\text{STC}}}{\text{SNR}_{\text{TDM}}} &= 10\log_{10}\left(\frac{\sigma^2_{\text{TDM}}}{\sigma^2_{\text{STC}}}\right) \\ &= 10\log_{10}(N_t)\ \text{dB}. \end{aligned} \tag{24}$$

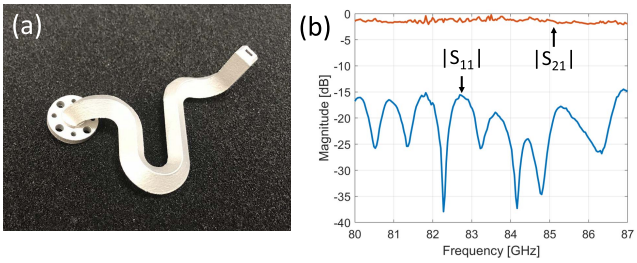

Fig. 4. Design and measurement of a single WR-12 waveguide bend. (a) Fabricated waveguide bend by DMLS. (b) Measured magnitude responses of S_{11} and S_{21}.

IV. Experiments With SDMMW Radar

A. Radar Prototype Design

The SDMMW radar prototype is designed using four commercial cost-effective SDRs (each has two Tx and two Rx ports), an external tunable LO with a 16-way power splitter to generate coherent stepped FMCW for all the Tx and Rx channels, a clock distributor to provide the baseband clock (10 MHz) and timing reference (1 PPS, pulse per second), some 90° and 180° RF couplers, 8 off-the-shelf mm-wave Tx mixers (81–86 GHz), 8 off-the-shelf mm-wave Rx mixers (81–86 GHz), and a metal-printed 8-by-8 waveguide array to form total 64 virtual channels. The SDRs are attached to a USB 3.0 interface of the host PC. Note that the aforementioned modules are selected to demonstrate the general functionalities of the proposed SDMMW multistatic architecture, which are not limited to any specific brands.

The baseband STC OFDM is designed to have 32 subcarriers, namely, $N_{\text{subc}} = 32$, and the baseband AD/DA sampling rate is 8 MS/s, resulting in an overall Tx/Rx data rate of 512 MB/s, namely, 8 MS/s × 8 Bytes per complex float sample × 8 channels, approaching the maximum throughput of a typical USB 3.0 interface. The IF input-output at SDRs is set to 700 MHz. The stepped FMCW sweeps from 13.4 to 14.2 GHz, which is generated by the external LO module. The total 100 equally spaced FMCW frequencies are used in the following experiment. The Tx (or Rx) mm-wave mixer functions as a ×6 multiplier and an upconverter (or a downconverter). Thus, the mm-wave operates at a center frequency of 83.5 GHz with a bandwidth of 4.8 GHz. The FMCW frequency step time is 500 μs where the dwell time is 400 μs that is necessary for a stable phase lock loop in the LO module, and the remaining 100 μs is for the STC OFDM waveform streaming.

The original Tx and Rx WR-12 ports of the mm-wave mixers are arranged in a square shape with an inter-port separation of 40 mm. Such a large separation is imposed by the physical dimension of the mm-wave mixers. To minimize

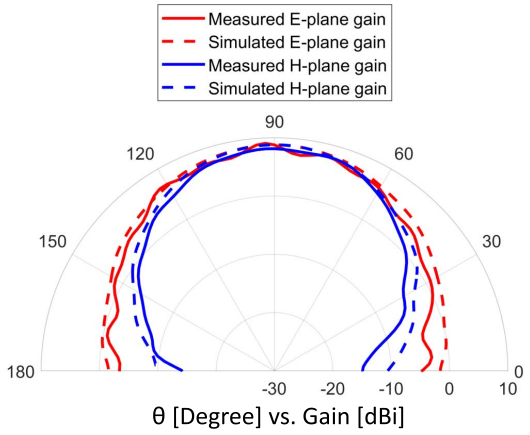

Fig. 5. Far-field gain patterns of the fabricated WR-12 waveguide bend.

the inter-port separation and reduce the sidelobe effect in mm-wave images, a waveguide bend is first fabricated by direct metal laser sintering (DMLS), as given in Fig. 4(a). Note that the UG-387/U flange is to be connected to the WR-12 port of the mm-wave mixer. As shown in Fig. 4(b), the measured magnitude of the reflection coefficient ($|S_{11}|$) is below -15 dB within the radar operating band and the averaged transfer gain ($|S_{21}|$) is -1.4 dB, showing a good fabrication quality with a low propagation attenuation. Additionally, the far-field gain patterns of the waveguide bend are simulated and measured. As shown in Fig. 5, the simulated and measured 3-dB beam widths at the E-plane are 65.5° and 73.4°, respectively. The simulated and measured 3-dB beam widths at the H-plane are 57.5° and 59.3°, respectively. The simulated main lobe gains at the E-plane and the H-plane are both 8.8 dBi, and the measured main lobe gains at the E-plane and the H-plane are 9.1 and 8.2 dBi, respectively.

The design and fabrication of a whole waveguide array with 16 parts are given in Fig. 6, where the eight Tx ports and eight Rx ports are aligned with the x-axis and z-axis, respectively. The waveguide array has an output inter-port separation of 9 mm. Fig. 6(a) shows the simulated model, where the simulation is to optimize the shapes of all the waveguide parts so that their transfer functions, namely, S_{21}, exhibit approximately the same responses in magnitude and phase. Fig. 6(b) shows the corresponding virtual MIMO array that consists of 64 channels. The final fabricated waveguide array is given in Fig. 6(c) where additional plastic parts are used to fix and align all the 16 waveguide bends.

The system parameters of the radar prototype are summarized in Table I, where $\Delta d = 9$ mm is the output interport separation, $D_0 = 36$ mm is the MIMO aperture dimension, BW $= 4.8$ GHz is the radar frequency bandwidth, and all the other parameters have been defined in previous sections.

B. Hardware-Related Specifications

In this section, the hardware-related specifications of the designed radar prototype are studied, which include Tx power, Rx noise figure (NF), and the receiving SNR. To study Tx power, the IF power transmitted from the SDR is first

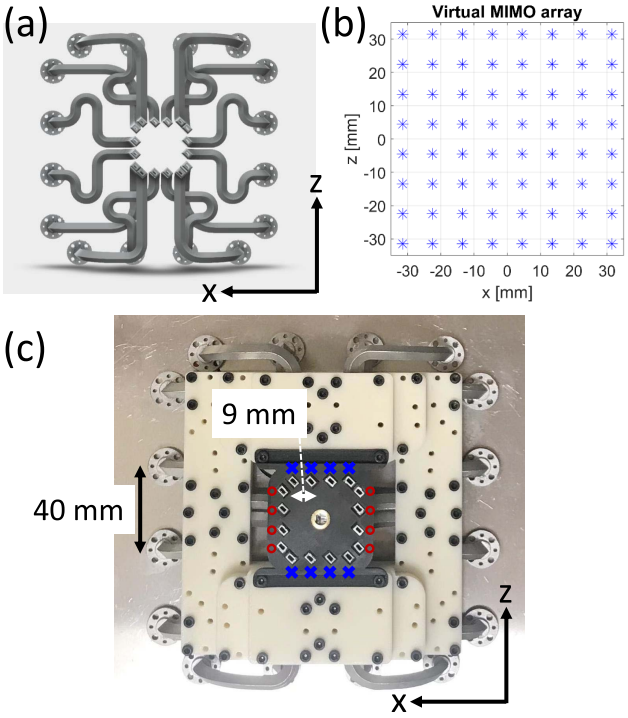

Fig. 6. Design and fabrication of the whole waveguide array with 16 waveguide bends (eight Txs and eight Rxs). (a) Simulated model. (b) Virtual MIMO array. (c) Fabricated waveguide array with additional plastic parts to fix and align all those 16 waveguide bends, where the transmitting and receiving ports are indicated by blue crosses and red circles, respectively.

TABLE I
SYSTEM PARAMETERS OF THE RADAR PROTOTYPE

Name	Value	Name	Value
N_{t}	8	Δd	9 mm
N_{r}	8	f_{c}	83.5 GHz
N_{c}	100	BW	4.8 GHz
N_{subc}	32	T_{d}	400 μs
D_0	36 mm	T_{a}	100 μs

measured, which is $P_{\mathrm{SDR}} = -25.5$ dBm. Considering the gains of RF couplers and the conversion gain of the Tx mm-wave mixer, the estimated Tx power is

$$\begin{aligned} P_{\mathrm{Tx}} &= P_{\mathrm{SDR}} + G_{0/90^\circ} + G_{0/180^\circ} + G_{\mathrm{Tx-Mixer}} \\ &= -25.5 - 3.2 - 4.7 + 33 \\ &= -0.4 \text{ dBm} \end{aligned} \tag{25}$$

where $G_{0/90^\circ} = -3.2$ dB is the gain of the $0/90^\circ$ coupler, $G_{0/180^\circ} = -4.7$ dB is the gain of the $0/180^\circ$ coupler, and $G_{\mathrm{Tx-Mixer}} = 33.0$ dB is the conversion gain of the Tx mm-wave mixer.

To estimate the Rx NF, all the NFs of the cascaded modules in the Rx chain need to be considered, which results in the

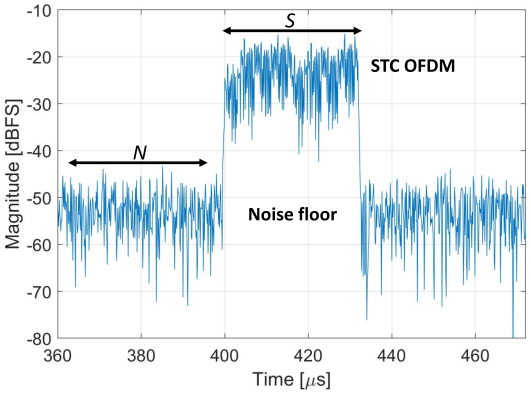

Fig. 7. Typical received STC OFDM waveform with thermal noise for the receiving SNR estimation.

overall NF of the Rx chain as

$$\begin{aligned}\mathrm{NF_{Rx}} &= 10\log_{10}\Bigg(\mathrm{NF_{Rx-Mixer}} + \frac{\mathrm{NF}_{0/180^\circ}-1}{G_{\mathrm{Rx-Mixer}}} \\ &\quad + \frac{\mathrm{NF}_{0/90^\circ}-1}{G_{\mathrm{Rx-Mixer}}G_{0/180^\circ}} \\ &\quad + \frac{\mathrm{NF_{SDR}}-1}{G_{\mathrm{Rx-Mixer}}G_{0/180^\circ}G_{0/90^\circ}}\Bigg) \\ &= 10.3\ \mathrm{dB} \end{aligned} \tag{26}$$

where $\mathrm{NF_{Rx-Mixer}} = 10.0$ dB is the NF of the Rx mm-wave mixer, $G_{\mathrm{Rx-Mixer}} = 10.0$ dB is the conversion gain of the Rx mm-wave mixer, $\mathrm{NF}_{0/180^\circ} = 4.7$ dB is the NF of the $0/180^\circ$ coupler, and $\mathrm{NF}_{0/90^\circ} = 3.2$ dB is the NF of the $0/90^\circ$ coupler.

To measure the receiving SNR, a standard corner reflector (Eravant SAJ-014-S1) with an edge length of 35.56 mm and an effective radar cross section (RCS) of 0.13 m^2 is used, which is placed 100-cm away in front of the MIMO aperture. The typical received STC OFDM waveform at each FMCW frequency step is given in Fig. 7. Thus, the receiving SNR can be estimated by

$$\begin{aligned}\mathrm{SNR} &= 10\log_{10}\left(\frac{\sum_{n\in S}|r[n]|^2}{\sum_{n\in N}|r[n]|^2}\right) \\ &= 28.8\ \mathrm{dB}\end{aligned} \tag{27}$$

where $r[n]$ is the typical received waveform and n is the sample index. The measured SNR is the power ratio between the STC OFDM samples (the set S) and the thermal noise samples (the set N), where both sets S and N contain the same number of measurement samples.

C. Imaging Experiments

The calibration of the radar prototype has to be performed before imaging any targets, which is to measure and compensate the phase and magnitude error among all MIMO channels to enable coherent multistatic operation [2]. In this experiment, the same corner reflector with an edge length of 35.56 mm is used as the calibrator, which is placed in the far-field of the MIMO aperture and facing the array center. In this case, the distance must be larger than

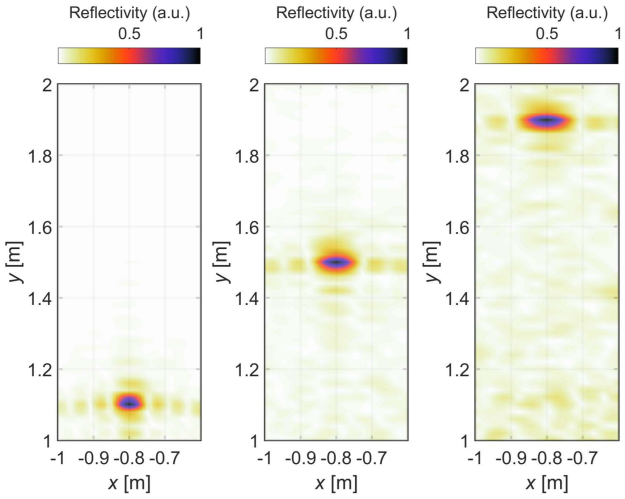

Fig. 8. Imaged corner reflector at different ranges, showing the effectiveness of the calibration method.

$((2f_cD_0^2)/c_0) \approx 72$ cm. Thus, the corner reflector is placed 150-cm away in front of the MIMO array. The calibration process can be described as

$$\tilde{\mathbf{g}} = (\mathbf{g} - \mathbf{g}_{\mathrm{BG}}) \cdot \left(\frac{\mathbf{g}_{\mathrm{C-SIM}}}{\mathbf{g}_{\mathrm{C-EXP}} - \mathbf{g}_{\mathrm{BG}}}\right) \tag{28}$$

where $\mathbf{g}_{\mathrm{BG}}$ is the background measurement in the absence of any object in front of the radar (note that the mutual coupling effect among the antenna elements in the measurement vector will be eliminated during background substraction); $\mathbf{g}_{\mathrm{C-EXP}}$ is the measured response of the calibrator at the far-field of the MIMO aperture; $\mathbf{g}_{\mathrm{C-SIM}}$ is the simulated response of the same calibrator; $(\cdot/\cdot)$ is the element-wise division operation to measure and compensate the phase and magnitude error for all MIMO channels at each frequency; $\mathbf{g}$ is any raw measurement vector before calibration; and $\tilde{\mathbf{g}}$ is the calibrated measurement vector for 3-D imaging processing. Considering the thermal drift might happen during radar operation, periodical calibration is necessary to avoid potential thermal-induced frequency drift and imaging reconstruction distortion.

To verify the effectiveness of the calibration scheme, additional measurements on the corner reflector with an edge length of 35.56 mm are performed. Fig. 8 shows the 2-D imaging reconstructions of the corner reflector at different ranges in the far-field of the MIMO aperture. As can be seen, the object is well-imaged and the imaged 3-dB size in the cross-range (x-axis) increases as the range extends, satisfying the theoretical imaging resolution as it will be described later in (29). Thus, calibration effectiveness is verified.

The PSF of the radar system is measured to see the focusing performance of the MIMO array. Fig. 9(a) shows the measured 3-D PSF at the range $R_0 = 100$ cm, and Fig. 9(b) shows the corresponding 1-D PSFs along the cross-range (x-axis), elevation (z-axis), and range (y-axis), respectively, where the 3-dB beamwidths are 58.3, 63.2, and 38.4 mm, respectively. To further evaluate the focusing performance of the radar system, the theoretical resolutions in the cross-range, elevation,

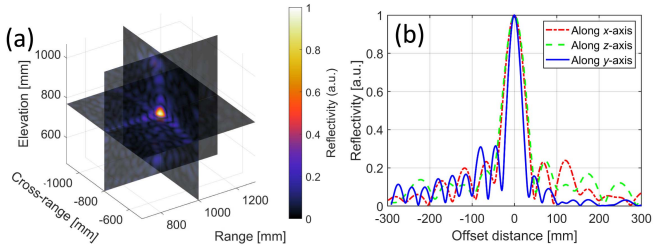

Fig. 9. (a) Measured 3-D PSF at the range 100 cm. (b) Corresponding 1-D PSFs along the cross-range (x-axis), elevation (z-axis), and range (y-axis), respectively, where the 3-dB beamwidths are 58.3, 63.2, and 38.4 mm, respectively.

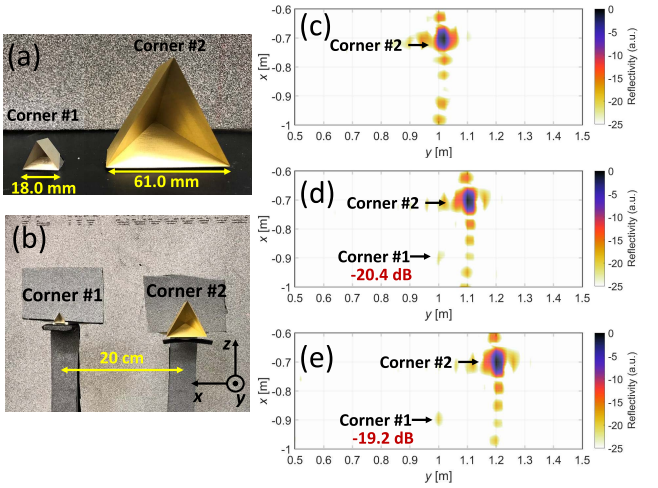

Fig. 10. Dynamic range evaluation of the SDMMW multistatic radar prototype. (a) Two corner reflectors used in the experiments. (b) Experimental setup of the two corners, separated by 20 cm in the cross-range. (c)–(e) 2-D reconstructed profiles along the range (x-axis) and cross-range (y-axis), where corner #1 is fixed at $y = 1.0$ m and corner #2 is placed at $y = 1.0$ m, $y = 1.1$ m, and $y = 1.2$ m, respectively.

and range are computed as follows:

$$\begin{aligned}\delta_{x/z} &= \frac{c_0 R_0}{2 f_c D_0} \\ &= 49.9 \text{ mm} \\ \delta_y &= \frac{c_0}{2\text{BW}} \\ &= 31.3 \text{ mm}. \end{aligned} \tag{29}$$

To evaluate the dynamic range of the radar prototype, more measurements are performed. Fig. 10(a) shows the two corner reflectors used in the experiments where corner #1 (Eravant SAJ-007-S1-0.71) has an edge length of 18.0 mm, corresponding to an effective RCS of 0.0085 m^2 at 83.5 GHz, and corner #2 (Eravant SAJ-024-S1) has an edge length of 60.0 mm, corresponding to an effective RCS of 1.0514 m^2 at 83.5 GHz. Those two objects are selected to ensure a large reflectivity contrast in mm-wave images, namely, to test a dynamic range >20 dB. Fig. 10(b) shows the experimental setup to image the two corner reflectors separated by 20 cm in the cross-range. Fig. 10(c)–(e) shows the 2-D reconstructed profiles along the range and cross-range, where corner #1 is fixed at $y = 1.0$ m and corner #2 is placed at $y = 1.0$ m, $y = 1.1$ m, and $y = 1.2$ m, respectively. As can be seen in Fig. 10(d) and (e), both the corners are well-imaged when they

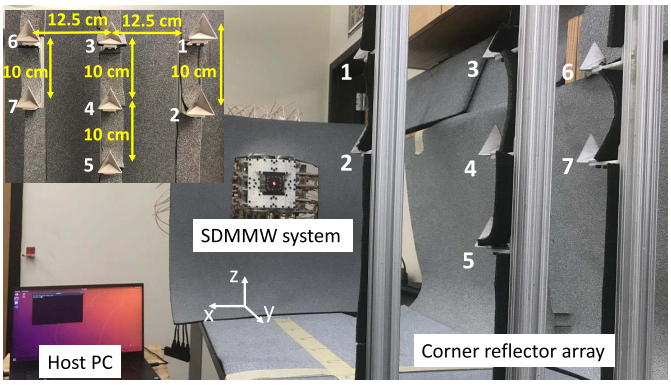

Fig. 11. SDMMW imaging experiment to detect an array of corner reflectors in 3-D.

are separated along the range, showing high dynamic range. However, in Fig. 10(c), corner #1 is hardly distinguished from corner #2 due to the sidelobe effect. This is because current multistatic array has an antenna element separation of 9 mm (greater than a half wavelength), which, however, is almost the smallest separation that can be achieved based on the waveguide bend structure. As a future effect to eliminate the sidelobe effect and achieve high dynamic range, the element separation can be reduced by designing a patch antenna array on a mm-wave PCB.

The software in the radar prototype is developed using Python 2.0 with customized application programming interface (API) functions which are to coordinate all the hardware modules for 3-D imaging. First, the SDRs are initialized by: 1) synchronizing the time of all SDRs to 0 at the arrival of the 1 PPS edge from the external clock distributor; 2) generating and caching the baseband STC OFDM waveform samples for each Tx in the random access memory (RAM) of the host PC; and 3) preloading the sensing matrices in RAM, which will be used in 3-D imaging reconstruction. Once initialized, all the MIMO channels will wait for the first measurement trigger controlled by the software. Note that the trigger interval needs to be matched with the FMCW sweeping rate that is $N_c \times (T_d + T_a) = 50$ ms per cycle. Thus, the trigger interval should be $N \times 50$ ms, N being any positive integer, where the first 50 ms is for radar waveform streaming and the following $(N-1) \times 50$ is the time period for imaging processing. In the experiment, the host PC uses i7-9750H processor with total 12 threads, where the averaged imaging processing time is ~340 ms. Thus, to allow sufficient time for imaging processing, $N = 10$ is selected, corresponding to an overall image formation rate of 2 fps (frames per second). Note that the current experiments mainly focus on imaging static objects due to the relatively slow frequency sweep of the external LO. However, using a much faster FMCW generator, real-time imaging with Doppler compensation is feasible, where 4-D (1-D velocity + 3-D object profile) object imaging can be achieved.

The experimental setup to image an array of corner reflectors is given in Fig. 11, where the corner reflectors are customized and fabricated by metal printing. The corner reflectors have an identical shape with an edge length of 36 mm. As can

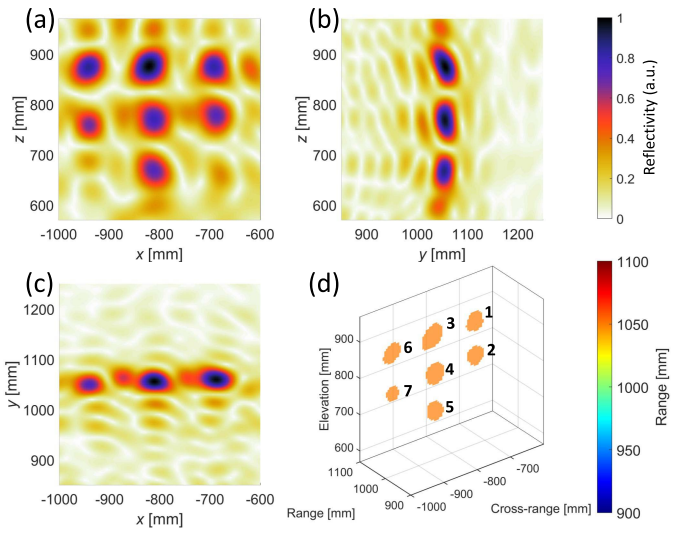

Fig. 12. First 3-D imaging reconstruction on the corner reflector array. (a)–(c) Object reflectivity images at the $x-z$, $y-z$, and $x-y$ planes, respectively. (d) Imaged object profile in 3-D with a display threshold of 0.45.

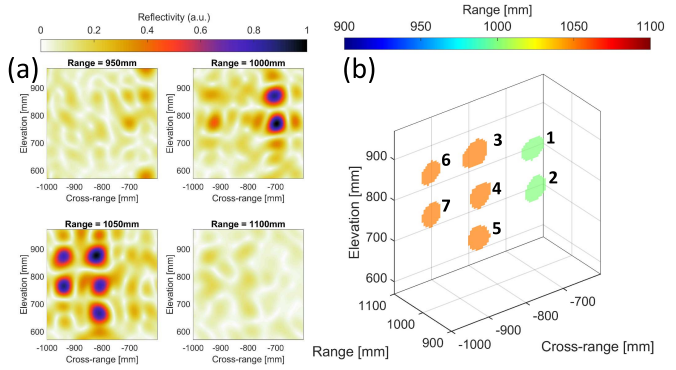

Fig. 13. Second 3-D imaging reconstruction on the corner reflector array. (a) Object reflectivity at different range planes. (b) Imaged object profile in 3-D with a display threshold of 0.45.

be seen in the inserted subplot of Fig. 11, the corner reflectors have a measured cross-range separation of 12.5 cm and an elevation separation of 10 cm. In the first imaging experiment, all the corner reflectors #1–#7 are placed at the range 105 cm. While in the second imaging experiment, corner reflectors #1 and #2 are located at the range 100 cm; while corner reflectors #3–#7 are placed at the range 105 cm. The 3-D imaging results of the corner reflector array in the first experiment are plotted in Fig. 12. The object reflectivity is plotted by different cuts at the $x-z$, $y-z$, and $x-y$ planes, as shown in Fig. 12(a)–(c), respectively. The imaged object profile in 3-D is presented in Fig. 12(d) where only the pixels with normalized reflectivity larger than 0.45 are displayed. Similarly, the 3-D imaging results in the second experiment are presented in Fig. 13, where Fig. 13(a) and (b) shows the reconstructed object reflectivity and profile, respectively. As can be seen from the experimental imaging results, all the corner reflectors are well-imaged and distinguished from each other in 3-D, showing a good imaging performance of the established radar prototype.

V. Conclusion

This article presents a new SDMMW multistatic radar system with efficient multiplexing for 3-D imaging applications. The general block diagram has been proposed with massive MIMO capability. Its signal model and imaging theory are developed to use STC OFDM for simultaneous MIMO transmission at the same time and frequency. An experimental prototype is designed to validate the feasibility of the proposed radar system, which operates at 83.5 GHz with a frequency bandwidth of 4.8 GHz. To achieve a small element separation and reduce the sidelobe effect, an 8-by-8 waveguide array is metal-printed to form 64 virtual channels with a small element separation of 9 mm. The experimental results have shown good imaging performance, giving great potential to design future cost-effective high-performance mm-wave imaging with efficient multiplexing.

References

[1] D. Bleh *et al.*, "*W*-band time-domain multiplexing FMCW MIMO radar for far-field 3-D imaging," *IEEE Trans. Microw. Theory Techn.*, vol. 65, no. 9, pp. 3474–3484, Sep. 2017.

[2] Q. Guo, Z. Wang, T. Chang, and H.-L. Cui, "Millimeter-wave 3-D imaging testbed with MIMO array," *IEEE Trans. Microw. Theory Techn.*, vol. 68, no. 3, pp. 1164–1174, Mar. 2020.

[3] S.-Y. Jeon *et al.*, "W-band FMCW MIMO radar system for high-resolution multimode imaging with time- and frequency-division multiplexing," *IEEE Trans. Geosci. Remote Sens.*, vol. 58, no. 7, pp. 5042–5057, Jul. 2020.

[4] H. Haderer, R. Feger, C. Pfeffer, and A. Stelzer, "Millimeter-wave phase-coded CW MIMO radar using zero- and low-correlation-zone sequence sets," *IEEE Trans. Microw. Theory Techn.*, vol. 64, no. 12, pp. 4312–4323, Dec. 2016.

[5] A. Santra, A. R. Ganis, J. Mietzner, and V. Ziegler, "Ambiguity function and imaging performance of coded FMCW waveforms with fast 4D receiver processing in MIMO radar," *Digit. Signal Process.*, vol. 97, Feb. 2020, Art. no. 102618.

[6] D. Schindler, B. Schweizer, C. Knill, J. Hasch, and C. Waldschmidt, "Synthetization of virtual transmit antennas for MIMO OFDM radar by space-time coding," *IEEE Trans. Aerosp. Electron. Syst.*, vol. 57, no. 3, pp. 1964–1971, Jun. 2021.

[7] D. Schindler, B. Schweizer, C. Knill, J. Hasch, and C. Waldschmidt, "MIMO-OFDM radar using a linear frequency modulated carrier to reduce sampling requirements," *IEEE Trans. Microw. Theory Techn.*, vol. 66, no. 7, pp. 3511–3520, Jul. 2018.

[8] C. Knill, F. Roos, B. Schweizer, D. Schindler, and C. Waldschmidt, "Random multiplexing for an MIMO-OFDM radar with compressed sensing-based reconstruction," *IEEE Trans. Microw. Wireless Compon. Lett.*, vol. 29, no. 4, pp. 300–302, Apr. 2019.

[9] D. Schindler, B. Schweizer, C. Knill, J. Hasch, and C. Waldschmidt, "An integrated stepped-carrier OFDM MIMO radar utilizing a novel fast frequency step generator for automotive applications," *IEEE Trans. Microw. Theory Techn.*, vol. 67, no. 11, pp. 4559–4569, Nov. 2019.

[10] P. Cruz, N. B. Carvalho, and K. A. Remley, "Designing and testing software-defined radios," *IEEE Microw. Mag.*, vol. 11, no. 4, pp. 83–94, Jun. 2010.

[11] C. Pfeffer, M. Jahn, R. Feger, R. Hüttner, and A. Stelzer, "A software defined radar platform for mm-wave sensing applications," in *Proc. 11th IEEE Eur. Radar Conf. (EuRAD)*, Oct. 2014, pp. 281–284.

[12] C. Pfeffer, R. Feger, and A. Stelzer, "A stepped-carrier 77-GHz OFDM MIMO radar system with 4 GHz bandwidth," in *Proc. Eur. Radar Conf. (EuRAD)*, Sep. 2015, pp. 97–100.

[13] H. Haderer, R. Feger, C. Pfeffer, and A. Stelzer, "Millimeter-wave phase-coded CW MIMO radar using zero-correlation-zone sequence sets," in *IEEE MTT-S Int. Microw. Symp. Dig.*, May 2015, pp. 1–4.

[14] R. Zhao, T. Woodford, T. Wei, K. Qian, and X. Zhang, "M-Cube: A millimeter-wave massive MIMO software radio," in *Proc. 26th Annu. Int. Conf. Mobile Comput. Netw. (MobiCom)*. New York, NY, USA: Association for Computing Machinery, Apr. 2020, pp. 1–14.

[15] M. Ettus and M. Braun, "The universal software radio peripheral (USRP) family of low-cost SDRS," in *Opportunistic Spectrum Sharing and White Space Access: The Practical Reality*. Hoboken, NJ, USA: Wiley, 2015, pp. 3–23.
[16] A. M. Wyglinski, D. P. Orofino, M. N. Ettus, and T. W. Rondeau, "Revolutionizing software defined radio: Case studies in hardware, software, and education," *IEEE Commun. Mag.*, vol. 54, no. 1, pp. 68–75, Jan. 2016.
[17] J. Guan, A. Paidimarri, A. Valdes-Garcia, and B. Sadhu, "3-D imaging using millimeter-wave 5G signal reflections," *IEEE Trans. Microw. Theory Techn.*, vol. 69, no. 6, pp. 2936–2948, Jun. 2021.
[18] J. Guan, A. Paidimarri, A. Valdes-Garcia, and B. Sadhu, "3D imaging using mmWave 5G signals," in *Proc. IEEE Radio Freq. Integr. Circuits Symp. (RFIC)*, Aug. 2020, pp. 147–150.
[19] S. S. Ahmed, "Microwave imaging in security—Two decades of innovation," *IEEE J. Microw.*, vol. 1, no. 1, pp. 191–201, Jan. 2021.
[20] H. Bolcskei, "MIMO-OFDM wireless systems: Basics, perspectives, and challenges," *IEEE Wireless Commun.*, vol. 13, no. 4, pp. 31–37, Aug. 2006.
[21] M. Baro and J. Ilow, "Space-time block codes based on diagonalized Walsh–Hadamard transform with simple decoupling," in *Proc. IEEE 72nd Veh. Technol. Conf.-Fall*, Sep. 2010, pp. 1–5.
[22] R. N. Mutagi, "Pseudo noise sequences for engineers," *IEEE Electron. Commun. Eng. J.*, vol. 8, no. 2, pp. 79–87, Apr. 1996.
[23] E. W. Weisstein. (2002). *Rectangle Function*. [Online]. Available: https://mathworld.wolfram.com
[24] C. A. Balanis, *Advanced Engineering Electromagnetics*. Hoboken, NJ, USA: Wiley, 2012.
[25] W. Zhang *et al.*, "Experimental results of a 3-D millimeter-wave compressive reflector antenna imaging system," *IEEE Antennas Wireless Propag. Lett.*, vol. 18, no. 1, pp. 24–28, Jan. 2019.
[26] A. Meta and P. Hoogeboom, "Signal processing for FMCW SAR," *IEEE Trans. Geosci. Remote Sens.*, vol. 45, no. 11, pp. 3519–3532, Oct. 2007.

Weite Zhang (Graduate Student Member, IEEE) received the B.Sc. and M.Sc. degrees in electrical engineering from Zhejiang University of Technology, Hangzhou, China, in 2014 and 2017, respectively. He is currently pursuing the Ph.D. degree in electrical engineering with Northeastern University, Boston, MA, USA.

His research interests include wireless communication and network, and millimeter-wave sensing and imaging systems.

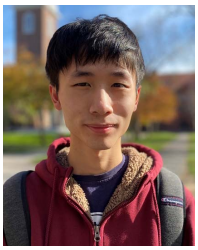

Yi Huang (Graduate Student Member, IEEE) received the B.Sc. degree in electrical engineering from Harbin Institute of Technology, Harbin, China, in 2019. He is currently pursuing the Ph.D. degree in electrical engineering with Northeastern University, Boston, MA, USA.

His research interests include RF/microwave, millimeter-wave engineering, computational electromagnetics, and wireless communication.

Juan Heredia-Juesas received the B.Sc. degree in telecommunications engineering, the M.Sc. degree in information technology and communications in mobile networks, and the Ph.D. degree in telecommunications engineering from the University of Oviedo, Oviedo, Spain, in 2009, 2010, and 2014, respectively.

He was a Post-Doctoral Research Associate with Northeastern University, Boston, MA, USA. His research interests include signal theory, signal processing, spectral analysis, machine learning, deep learning, and imaging, optimization, and distributed algorithms.

Jose A. Martinez-Lorenzo (Senior Member, IEEE) received the B.S. and M.S./Ph.D. degrees from the University of Vigo, Vigo, Spain, in 2002 and 2005, respectively.

He is currently an Associate Professor with the Department of Mechanical and Industrial Engineering and the Department of Electrical and Computer Engineering, Northeastern University, Boston, MA, USA. He is also the Director of Sensing Imaging Control and Actuation Laboratory, Northeastern University. He has authored over 200 technical journal and conference papers. His research interests include high-capacity sensing and imaging systems.

Dr. Martinez-Lorenzo was a recipient of the 2017 NSF Early CAREER Award. He also serves as an Associate Editor for the IEEE TRANSACTIONS ON ANTENNAS AND PROPAGATION.